



2nd Advanced Optical Metrology Compendium

Advanced Optical Metrology

Geoscience | Corrosion | Particles | Additive Manufacturing: Metallurgy, Cut Analysis & Porosity



EVIDENT
OLYMPUS

WILEY

The latest eBook from **Advanced Optical Metrology**.
Download for free.

This compendium includes a collection of optical metrology papers, a repository of teaching materials, and instructions on how to publish scientific achievements.

With the aim of improving communication between fundamental research and industrial applications in the field of optical metrology we have collected and organized existing information and made it more accessible and useful for researchers and practitioners.

EVIDENT
OLYMPUS

WILEY

Cathodes Coating Layer with Li-Ion Diffusion Selectivity Employing Interactive Network of Metal-Organic Polyhedras for Li-Ion Batteries

You Jin Kim, So Yeon Ko, Suji Kim, Kyung Min Choi,* and Won-Hee Ryu*

Surface modification of cathodes using Ni-rich coating layers prevents bulk and surface degradation for the stable operation of Li-ion batteries at high voltages. However, insulating and dense inorganic coating layers often impede charge transfer and ion diffusion kinetics. In this study, the fabrication of dual functional coating materials using metal-organic polyhedra (MOP) with 3D networks within microporous units of Li-ion batteries for surface stabilization and facile ion diffusion is proposed. Zr-based MOP is modified by introducing acyl groups as a chemical linkage (MOPAC), and MOPAC layers are homogeneously coated by simple spray coating on the cathode. The coating allow the smooth transport of electrons and ions. MOPAC effectively suppress side reactions between the cathode and electrolyte and protect active materials against aggressive fluoride ions by forming a Li-ion selective passivation film. The MOPAC-coated Ni-rich layered cathode exhibited better cycle retention and enhanced kinetic properties than pristine and MOP-coated cathodes. Reduction of undesirable gas evolution on the cathode by MOPAC is also verified. Microporous MOPAC coating can simultaneously stabilize both the bulk and surface of the Ni-rich layered cathode and maintain good electrochemical reaction kinetics for high-performance Li-ion batteries.

1. Introduction

Designing lithium-ion batteries (LIBs) with high energy density and stability simultaneously has been pivotal for future electronic devices and electric vehicles.^[1] $\text{LiNi}_x\text{Co}_y\text{Mn}_z\text{O}_2$ (NMC) and $\text{LiNi}_x\text{Co}_y\text{Al}_z\text{O}_2$ (NCA) ($x+y+z = 1$ and $x \geq 8$), two Ni-rich layered cathodes (NLCs), are designed using cathode materials with exceptionally high capacity and working potential, and low-cost Ni compared to conventional LiCoO_2 cathodes.^[2] The high Ni content imparts a high specific capacity of more than

200 mAh g⁻¹ of the cathode due to the $\text{Ni}^{2+}/^{4+}$ redox reaction at a high working voltage; this is regardless of restraining at the top of the $\text{O}^{2-} 2p$ band and eventually leads to a high energy density of the cell.^[3] However, NLCs have a poor cycling life, particularly at the highly delithiated state, owing to severe degradation by side reactions (electrolyte decomposition) on the cathode surface. High-valence Ni ions (Ni^{3+} , Ni^{4+}) at the highly delithiated state promote the formation of the unwanted disordered rock salt phase near the surface and resistive cathode-electrolyte interphase (CEI) layer. This phase aggravates stability and charge transfer between active materials, thereby degrading cell performance.^[4] Therefore, the surface stabilization of NLCs to prevent degradation and interfacial side reactions is essential for acquiring high energy density and long-term stability.

Studies have demonstrated the protection of NLCs by surface coating. Dense coating layers passivate the cathode surface against electrolyte side reactions but nonporous insulating materials hinder Li^+ transport across the electrode and electrolyte, and electron transfer via the coating layer from/to conductive carbon and current collectors. Metal-organic frameworks (MOFs), a type of porous material, are considered coating materials due to their i) exceptional porosity ($> 1000\text{--}10000 \text{ m}^2 \text{ g}^{-1}$), ii) stable and rigid structure formed by the coordination of metal ions and organic ligands, and iii) flexibility controlled by functional groups.^[5] Although multiple attempts have been made to introduce MOFs as a bifunctional coating agent for cathode protection and selective Li ion transport pathways, it has not been feasible because i) their microcrystals prevent the formation of a homogeneous film on the cathode^[6] and ii) large MOF particles form a thick layer impeding charge transfer and decreasing volumetric energy density.

Metal-organic polyhedra (MOP), a class of emerging porous materials, are a potential substitute for MOF since they have similar pore structures. However, each pore in MOP can be isolated by removing the electrostatic interaction between their unit cells.^[7] MOP unit cells interact with surfactants and increase their interaction with the aqueous medium. They are homogeneously dispersed in volatile solvents and uniformly deposited to form a thin film by the solution-based spray

Y. J. Kim, S. Y. Ko, S. Kim, K. M. Choi, W.-H. Ryu
Department of Chemical and Biological Engineering
Sookmyung Women's University
100 Cheongpa-ro 47-gil, Yongsan-gu, Seoul 04310, Republic of Korea
E-mail: kmchoi@sookmyung.ac.kr; whryu@sookmyung.ac.kr
K. M. Choi, W.-H. Ryu
Institute of Advanced Materials and Systems
Sookmyung Women's University
100 Cheongpa-ro 47-gil, Yongsan-gu, Seoul 04310, Republic of Korea

 The ORCID identification number(s) for the author(s) of this article can be found under <https://doi.org/10.1002/smll.202206561>.

DOI: 10.1002/smll.202206561

coating process.^[8] Microporous MOP has merits as a spray coating material to stabilize cathodes: i) MOP pore sizes can be controlled for selective Li⁺ diffusion while preventing the same for unwanted salts in electrolytes (e.g., PF⁶⁻).^[5b,9] Facile Li⁺ transport through MOP-coated layers stabilizes the cathode surface and prevents the transition of layered cathodes to other phases (spinel or rock salt). ii) The open pores of thin layered MOP at the cathode surface enables Li⁺ diffusion unlike dense and clogged coating layers of the conventional metal oxide coating.^[10] iii) MOP films directly sprayed on the electrode surface act as the active material route.

In this study, we proposed a facile spray-coating method for fabricating a coating layer on an NLC using microporous MOP networks for selectively transporting Li⁺ ions in LIBs. We modified Zr-based MOP with alkyl chains to make a homogeneous and microporous thin film (Figure 1). The direct coating on the cathode forms a preconnected pathway for ions between the cathode and current collector irrespective of electron transport through the insulating MOP layer. Zr-based MOP with sizes below 2 nm and alkyl-based surfactants maintain their structure and microporosity in the solution.^[10–11] Therefore, Zr-based MOP spray coating materials are stable during electrochemical reactions. We have synthesized MOP [Cp₃Zr₃O(OH)₃]₄[BDC-NH₂]₆[(C₂H₅)₂NH₂]₂Cl₆ and linked them with acyl chloride to form 3D networks. The chemical formula of the unit forming the network is [Cp₃Zr₃O(OH)₃]₄[BDC-NH]₆ [(C₂H₅)₂NH₂]₂Cl₆[C₆H₈ClO₂]_x (MOPAC). The characteristics of MOPAC layers were studied by investigating the morphology, thickness, homogeneity, composition, and ion selectivity. The electrochemical performance of MOPAC-coated cathodes was evaluated; the ex situ characterization of gases evolved at the cathode was carried out to verify its gas suppression capability. The development of a unique microporous coating material using this metal-organic material is a breakthrough for designing high-performance and safe LIBs.

2. Results and Discussion

The synthesis of MOPAC, and the fabrication of MOPAC-coated cathode are shown in Figure 2a. Zr-based MOP was prepared from Cp₂ZrCl₂ and 2-aminoterephthalic acid (H₂BDC-NH₂). Acyl chloride, as linkers, is chemically bonded to MOP to form a mesoporous 3D structure. MOPAC is coated on the NLC by the direct spray process. The synthesized MOP crystals are analyzed by powder X-ray diffraction (PXRD) as shown in Figure 2b showing high crystallinity with a structure similar to the reported structure.^[8b] The presence of the impurities remaining in the MOP pores makes the intensity different from simulated PXRD patterns, but the similar positions of diffraction peaks show the basal structure of the material is the same. After the addition of acyl chloride to MOP, highly crystalline cubic MOP of sizes 10 μm were altered as shown in Figure S1 (Supporting Information). The presence of acyl chloride in MOPAC is identified by ¹H-nuclear magnetic resonance (NMR) spectroscopy. Aromatic protons showed chemical shifts at 8.16, 8.13, and 8.01 ppm (a, b, and c in Figure 2c), and aliphatic protons showed chemical shifts at 2.2 and 1.4 ppm (d and e in Figure 2c). The integration ratio for aromatic to aliphatic protons was 1:4 demonstrating that acyl chloride was added to every amine group of MOPAC. A comparison between MOPAC and MOP by Fourier-transform infrared spectroscopy (FT-IR) spectroscopy revealed the disappearance of the amine group and appearance of the secondary amide group in MOPAC; this indicated that acyl chloride binds to amine in MOP as shown in Figure 2d. The existence of amino group can be analyzed by ν(C-N) bands which were observed at 1340 cm⁻¹. In particular, the appeared secondary amide peaks after binding acyl chloride to amine in MOP were observed at 1544 and 1350 cm⁻¹ that corresponds to the vibration of δ(C-N)+δ(CNH) and δ(NH)+δ(OCN), respectively.

The porosity of MOP and MOPAC was compared using N₂ adsorption at 77 K. Figure 2e shows a Type-I isotherm of

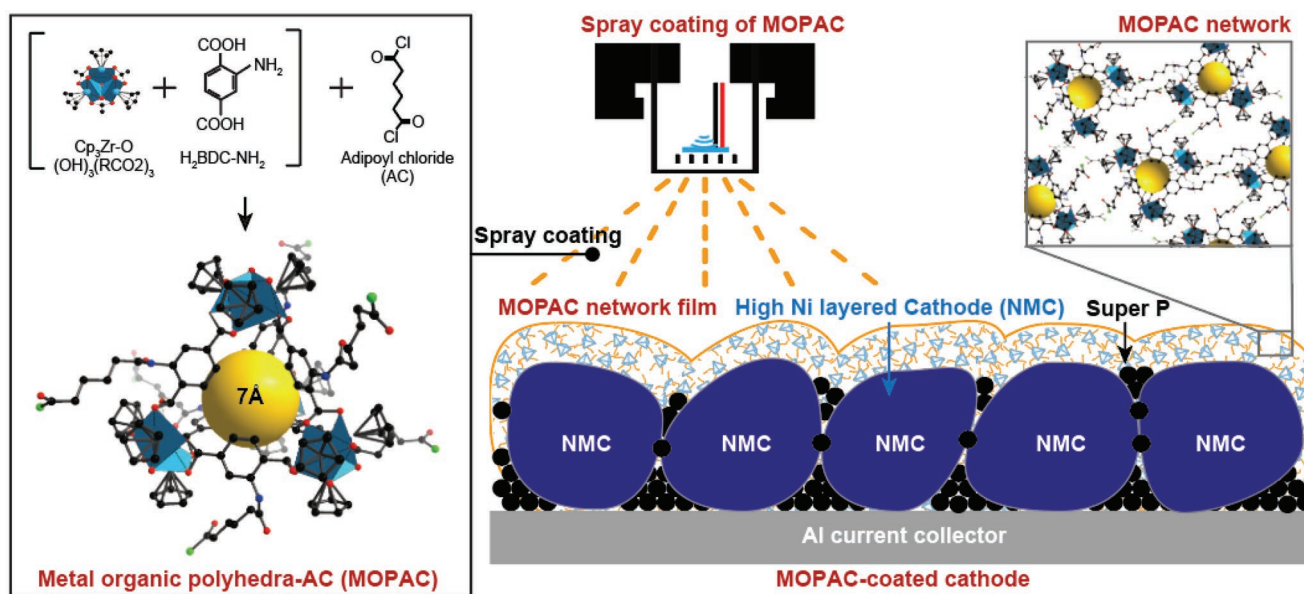


Figure 1. Schematic illustrations of the MPOAC-coated NMC cathode.

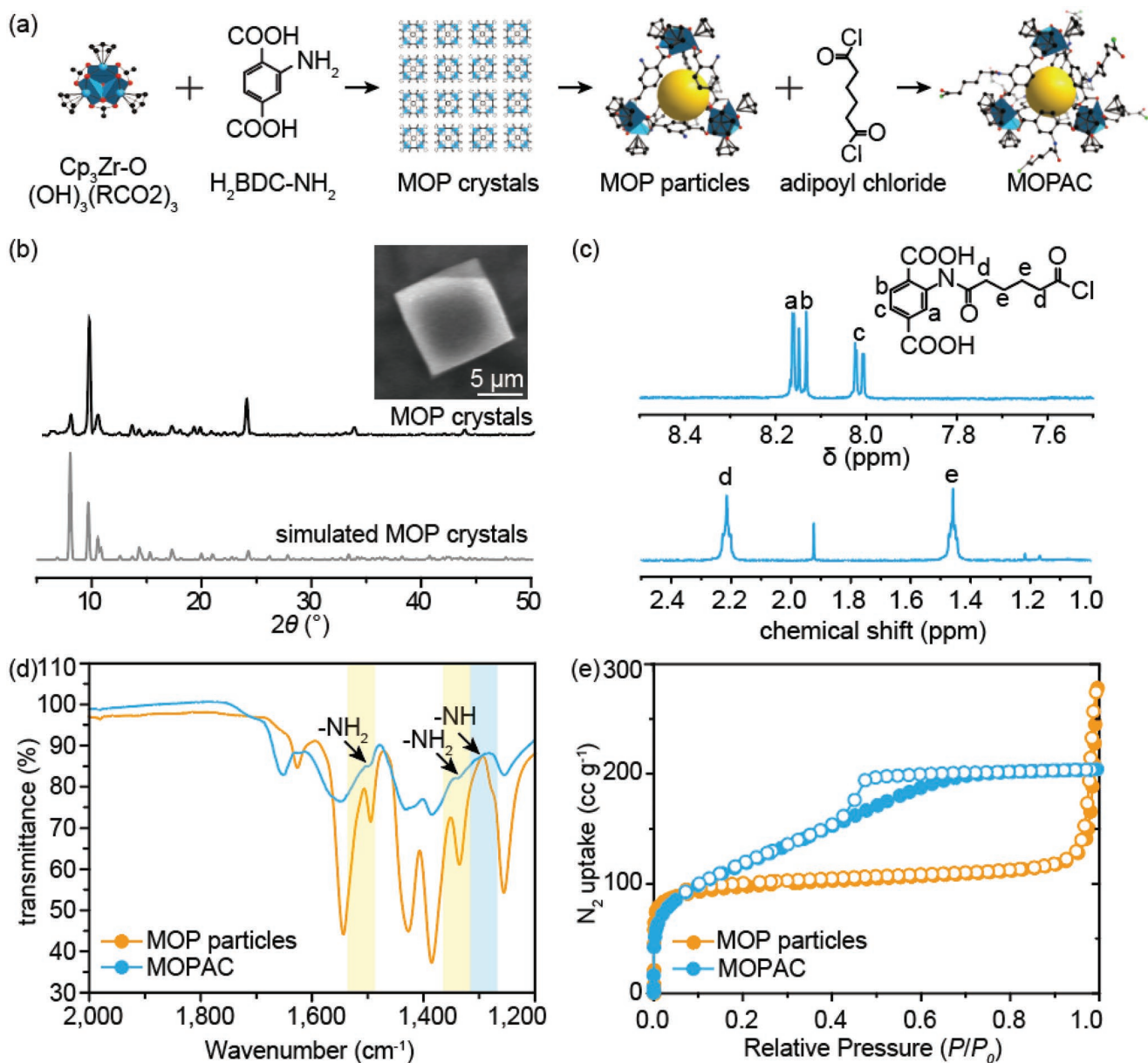


Figure 2. a) Schematic illustrations of MOPAC synthesis. b) XRD spectrum of MOP crystals and simulated MOP crystals. SEM image of synthesized crystalline MOP crystals. c) ^1H NMR spectrum of MOPAC. d) FT-IR spectra of MOP and MOPAC. e) N_2 sorption of MOP and MOPAC.

MOP indicating the presence of abundant micropores. The Langmuir surface area of MOP and MOPAC were 36745 and 384.65 $\text{m}^2 \text{g}^{-1}$, respectively, as indicated in Table S1 (Supporting Information). Apart from retaining the micropores, MOPAC also has mesopores. The pore size distribution of MOP and MOPAC calculated by non-local density functional theory (NLDFT) is shown in Figure S2 (Supporting Information). The micropores of MOP and MOPAC are 1.0–2.0 nm, and the mesopores of MOPAC are 4 nm. It is speculated that mesopores were formed due to the 3D network between acyl groups and MOP in MOPAC.

MOPAC dissolves completely in methanol to form a homogeneous dispersion as shown in Figure 3a which is essential for fabricating a thin film using the spray coating method. The

homogeneity of this solution was retained for over a year. The solution was sprayed on the NMC cathode that was placed on a hotplate at a temperature of 50 $^\circ\text{C}$ to form the MOPAC film. The solution was sprayed every 5 s by maintaining the distance between the cathode and spray gun at 15 cm. The surface morphology of the MOPAC-coated NMC cathode analyzed by scanning electron microscope (SEM) is macroscopically similar to the pristine NMC cathode as shown in Figure 3b. However, the cross-sectional image proves the presence of a uniformly coated 20 nm thick MOPAC film on the entire cathode surface as shown in Figure 3c. The existence of the MOPAC layer was also confirmed by energy dispersive spectrometer (EDS) mapping as shown in Figure 3d. The images confirm well-distributed Zr, Mn, and Ni throughout the MOPAC-coated NMC

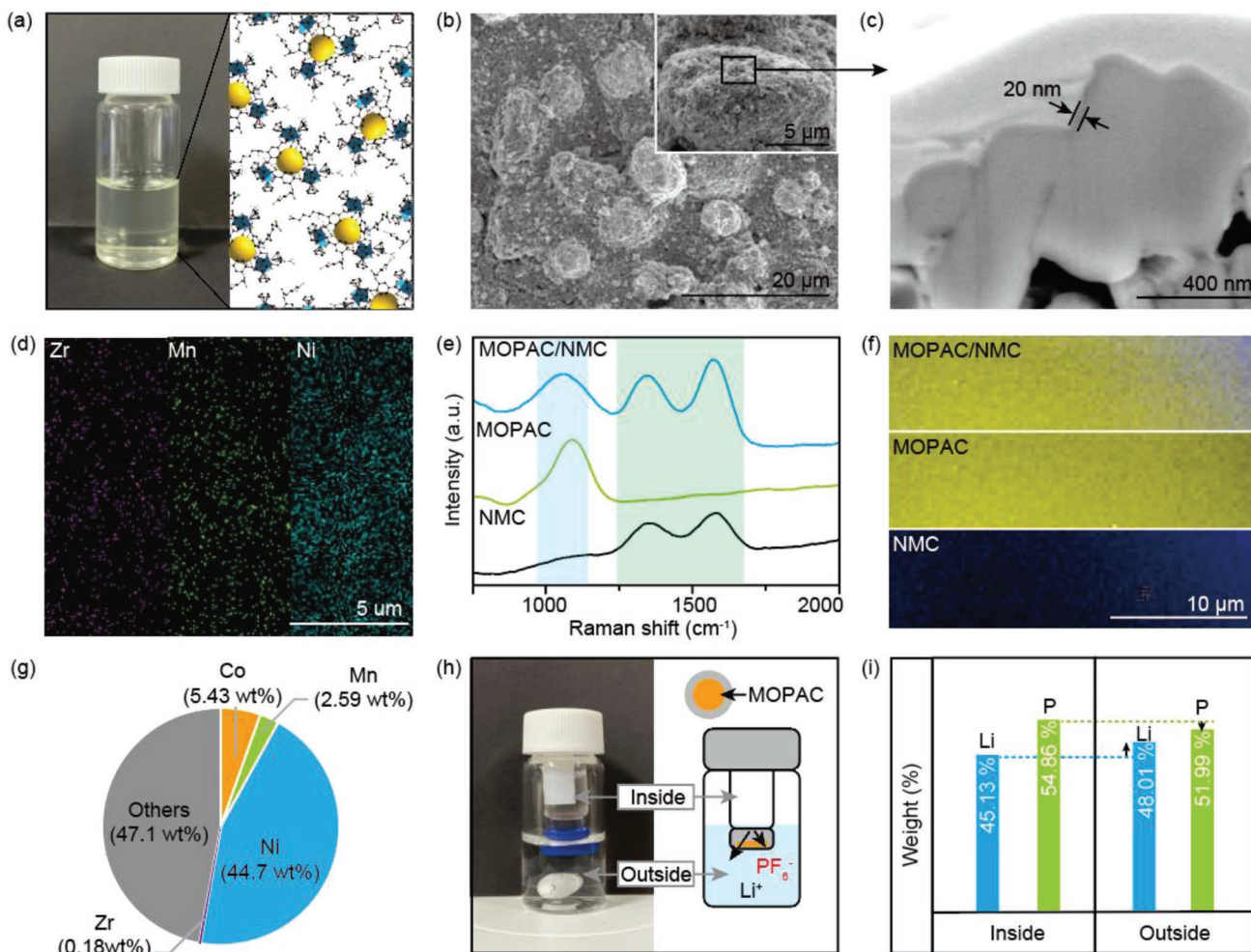


Figure 3. Material characterizations of MOPAC coated NMC. a) The image and schematic illustration of MOPAC solution. b) SEM images of the MOPAC/NMC surface. c) SEM-FIB image of MOPAC/NMC. d) EDS mapping images of MOPAC/NMC. e) Raman spectra of NMC, MOPAC, and MOPAC/NMC. f) Raman mapping images of NMC, MOPAC, and MOPAC/NMC. g) ICP-OES data of MOPAC/NMC. h) Image and schematic illustration of penetration experiment. i) ICP-OES data of MOPAC coated separator before and after electrolyte penetration.

cathode; Zr is present in MOPAC, and Mn and Ni are present in NMC. Raman spectroscopy also further proved the existence of MOPAC on the NMC electrode as shown in Figure 3e. Peaks at 1344 and 1573 cm^{-1} represent carbon having dangling bonds of disordered graphite (D-band) and sp^2 -bonded carbon-carbon stretching in graphite sheets (G-band) in NMC, respectively. The peak at 1058 cm^{-1} represents benzene ring deformation in terephthalates in MOPAC.^[12] Raman mapping images show that MOPAC (presented as yellow) is homogeneously coated on NMC (presented as blue) as shown in Figure 3f. The amount of MOPAC coated on NMC and compositional analysis on the coating layer was revealed by thermogravimetric analysis (TGA) and inductively coupled plasma-optical emission spectroscopy (ICP-OES) analysis as shown in Figure 3g. 0.2 wt.% of Zr is present in MOPAC film indicating that 0.75 wt.% of MOPAC was coated on NMC. This also verified that the MOPAC film is successfully deposited on the NMC cathode surface by spray coating.

Selective and fast Li^+ transport through the MOPAC film is crucial to enhance charge transfer reaction kinetics and

stabilize the cathode-electrolyte interface against reactions with solvents. Ion selectivity of the MOPAC film was elucidated by comparing the relative amount of Li^+ and PF_6^- in the electrolyte after their diffusion through the film. The experimental setup of ion diffusion is shown in Figure 3h. The LiPF_6 electrolyte was placed in a small vial and sealed by a cap equipped with a MOPAC-coated membrane filter. The vial was placed upside down and soaked in a large vial containing DMC devoid of Li^+ and PF_6^- ions. We anticipated that ions in the small vial would diffuse to the large vial through the MOPAC-coated filter. After 1 day, the amount of the ions diffused into the large vial solution was quantified by inductively coupled plasma-optical emission spectroscopy (ICP-OES). Li^+ and PF_6^- in the solvent after diffusion were 48.01% and 51.99%, respectively as shown in Figure 3i. Compared with the initial amount of Li^+ (45.13%) and PF_6^- (54.86%) inside the small vial, the amount of Li^+ increased while that of PF_6^- significantly decreased. Thus, the MOPAC film diffuses Li^+ selectively than PF_6^- , indicating that it can act as an ion-selective coating layer between the cathode and electrolyte.

We selected an NMC cathode with high Ni content ($\text{LiNi}_{0.83}\text{Mn}_{0.06}\text{Co}_{0.11}\text{O}_2$) with poor cyclic performance to study the effect of MOPAC coating on the electrochemical performance of NLCs. Charge and discharge curves for NMC and MOPAC/NMC cathodes at a rate of 0.1 C (1C = 250 mAh g^{-1}) from 2.5 to 4.3 V were evaluated after 100 cycles as shown in Figure 4a. Both electrodes showed the same reformation in all charge and discharge curves without any additional redox plateau of MOPAC/NMC after 100 cycles. This established the electrochemical inactivity of the MOPAC film during the cycling process. The NMC electrode has the 1st discharge capacity of 201 mAh g^{-1} , whereas the MOPAC/NMC electrode has a slightly larger 1st discharge capacity of 215 mAh g^{-1} . The first capacity loss in the NLC relates to the irreversible structural transition of cathodes and the continuous formation of surface impurity by losing active Li^+ .^[13] In addition, the trace amount of PF_6^- and HF in LiPF_6 continuously destructs the cathode surface; this exacerbates lithium loss and transition to the rock salt phase. The cathode surface protection by the MOPAC film effectively prevents the surface structure degradation and interfacial side reactions during the 1st cycle.^[14] The MOPAC film with microporous MOP particles connected by organic linkers allows selective Li^+ transport from the electrolyte to the surface and deters harmful species. MOPAC-coated NMC suppressed the active Li^+ loss by protecting the cathode surface and increased the less polar Li^+ ion diffusion rate through selective pathways. NMC and MOPAC/NMC electrodes showed discharge capacities of 143 and 151 mAh g^{-1} , respectively, after 50 cycles with the same discharge capacity retention rate as the initial cycle. After the 100th cycle, the discharge capacity of the NMC cathode drastically decreased to 100 mAh g^{-1} with a capacity retention rate of 52% due to the cathode and electrolyte degradation.^[15] By contrast, the MOPAC/NMC cathode maintained a high discharge capacity (126 mAh g^{-1}) even after 100 cycles; it also showed higher reversible charge capacities at different cycles as compared to those of the NMC cathode. The capacity loss of the NLC at its highly delithiated state is suppressed owing to the nanosized Zr domain as the surface stabilizer on the sustainable MOPAC film. Zr on the NLC surface enhances the NMC stability and inhibits the formation of oxygen vacancies at high voltages by forming strong Zr–O bonds at the bulk.^[16] The MOPAC film having abundant nanosized Zr clusters in MOP protects the cathode surface by reducing the unwanted Ni^{2+} generated at a highly delithiated state and maintaining the O3 layered structure.^[17] The film acts as a stable Li^+ conductor and surface stabilizer for reversible Ni redox reactions at a high voltage.

The cyclic performance and coulombic efficiency of NMC, MOP/NMC, and MOPAC/NMC cathodes at 0.1 C are shown in Figure 4b. After 100 cycles, the capacity retention of NMC and MOP/NMC cathodes are 52% and 49%, respectively, whereas the same for the MOPAC/NMC cathode is highest at 61%. The lowest value of MOP/NMC may result from the high ionic resistance of MOP layers due to localized aggregated MOP particles on the cathode surface due to the absence of acyl chloride. Alternately, the sprayed MOPAC film is well dispersed and adheres strongly to the entire electrode without aggregation because MOP-bonded acyl molecules prevent aggregation and induce homogeneous distribution. At the initial cycle, cou-

lombic efficiency values of NMC and MOPAC/NMC cathodes were 92% and 91%, respectively, which reached over 97% after 100 cycles. These similar values indicated the enhancement in Li^+ transport through the nonresistive coating layer resulting in the reversible capacity of MOPAC/NMC. The MOP/NMC electrode showed 88% of reduced coulombic efficiency at the initial cycle which was lower than both NMC and MOPAC/NMC electrodes. This is because of the high ohmic resistance and irreversible capacity due to limited Li^+ diffusion through aggregated MOP on the cathode surface. Acyl chloride increases MOPAC dispersion which helps Li^+ diffusion on the electrode.

The differential capacity of NMC and MOPAC/NMC cathodes at 2.5–4.3 V for comparing their phase changes is shown in Figure 4c. Three redox couple peaks in each cathodic/anodic area of both cathodes indicate the phase transition of the layered Ni-rich structure to the spinel/rock salt structure.^[18] The NMC cathode exhibited large peak shifts at high voltages and a rapid decrease in the intensity of cathodic/anodic regions after repeated cycles indicating an irreversible phase transition to the rock salt-like phase.^[19] This transition initiates near 4.20 V and forms weak covalent bonds between the transition metal and oxygen.^[20] The charge and discharge peaks of the NMC cathode due to irreversible phase transition are centered at 4.15 and 4.19 V at a small voltage gap of 0.04 V for the 2nd cycle, whereas the large peak shift at a low voltage caused the disappearance of the original peak after the 100th cycle. The peak disappearance at 4.25 V for the cathode after the 100th cycle indicates the destroyed layered structure of the NLC causing rapid capacity decrease and large overpotential at the cathode interface.^[21] Alternately, the MOPAC/NMC electrode showed lower voltage gap change from 0.03 to 0.04 V after the 100th cycle. Charge and discharge peaks at 4.18 and 4.15 V for the 2nd cycle slightly shifted to 4.21 and 4.09 V, respectively, even after the 100th cycle, indicating that the layered structure in the Ni-rich cathode remains intact with no drastic phase change.

The ohmic resistance of both electrodes (NMC and MOPAC/NMC) after 100 cycles was calculated by IR drop measurements between the end of the charge potential and the start of the discharge potential (Figure 4d). The initial IR drop of NMC and MOPAC/NMC cathodes was 28.14 and 38.95 mV, respectively. The slightly larger IR drop of the MOPAC/NMC electrode at the initial cycle was attributed to the inherent properties of organic species in MOPAC. The lower IR drop values of the MOPAC/NMC electrode after the 50th and 100th cycles were 146.78 and 183.68 mV, respectively, compared to the higher values of the NMC electrode (50th cycle = 238.97 mV, 100th cycle = 397.98 mV). The rapid increase in IR drop of NMC after repeated cycles is caused by the passivated outer cathode surface that forms the resistive cathode electrolyte interfacial (CEI) layer; this limits Li^+ diffusion and induces high ohmic polarization of active materials.^[14c,22] This increased IR drop deteriorates the energy density and electrochemical performance of the cell.^[11a,23] The MOPAC film significantly reduces instant ohmic resistance by improving the surface conductivity of Li^+ and interfacial stability for facile charge transport.

The overall resistance within the cell was compared by electrochemical impedance spectroscopy of each sample electrode after 100 cycles (Figure 4e). The bulk resistance (R_s) and charge-transfer resistance (R_{ct}) of NMC and MOPAC/NMC electrodes

were investigated by equivalent circuits using Nyquist plots at the 100th cycle. R_s is determined from the internal resistance and electron conductivity of the bulk materials: the electrolyte, separator, and electrode. R_{ct} is linked to the semicircle at a low frequency affected by the electrochemical reaction which is changed by the surface coating or phase transition.^[24] R_s increases with the number of cycles due to electrolyte depletion and microcrack formation, and R_{ct} increases due to sluggish lithiation induced by the structural change.^[25] The NMC electrode exhibits nearly two-fold higher impedance values ($R_s = 708 \Omega$ and $R_{ct} = 51.89 \Omega$) than those of the MOPAC/NMC electrode ($R_s = 3.01 \Omega$ and $R_{ct} = 25.75 \Omega$), indicating severe degradation of the structure, particle-to-particle contact, and interfacial charge transfer of the NMC electrode.^[26] The MOPAC film enhanced the electrochemical kinetics of electrons and ion transport, which decreased the overall cell resistance. ALD, a uniform coating process, coats each particle with a thin layer to stabilize the cathode surface, but a thick coating layer using insulating metal oxides reduces ion conductivity between particles.^[27] Direct MOPAC coating on the cathode surface instead of the cathode materials enhances the Li^+ migration to the cathode surface without any interparticle resistance. The connection between the cathode materials and conductive carbon prior to the surface coating should be effective to facilitate both electron and ion transport.

To examine the kinetic properties of the MOPAC film under fast cycling, the cycle performance of NMC and MOPAC/NMC electrodes at a high C-rate of 1.0 C (250 mA g^{-1}) was investigated (Figure 4f). An acyl chloride-coated NMC (AC/NMC) and MOP/NMC electrodes were evaluated initially. NMC showed initial activation for several cycles due to high ohmic resistance applied by a sudden large current, and its capacity retention rate was 58%. The initial capacity of AC/NMC increased rapidly up to 213 mAh g^{-1} and irreversibility decreased to 166 mAh g^{-1} . This drastic decrease in capacity is due to the reaction between active materials of NMC and hydrochloric acid (HCl) in the electrolyte.^[28] Acyl chloride hydrolyzes to form carboxylic acid and HCl.^[29] The rapid dissolution of Li and transition metals from NMC by HCl, formed by acyl chloride hydrolysis, leaches the electrode.^[30] Therefore, the AC/NMC electrode showed very low cycle performance at a high current. The MOP/NMC electrode showed the initial discharge capacity as 0 for several cycles at a high rate of 1.0 C. This is because of the limited Li^+ diffusion to the aggregated site of the MOP-coated layer at the cathode surface. Even after initial activation, the high overpotential applied to the surface aggregated MOP layer resulted in a low cycle performance than NMC. Alternately, MOPAC/NMC showed the highest cycle performance of 68% compared to the initial capacity due to the favorable chemical combination to form a stable composite. The composite also showed the least activation cycle, highest specific capacity, and highest capacity retention even at a high current density due to several factors: i) the smallest overpotential applied to the surface coating layer, ii) fast charge transport to the cathode surface, and iii) protection of the layered NMC structure for multiple cycles.

CV curves between 3.0 and 4.5 V under different scan rates from 0.1 to 1.0 mV s^{-1} for NMC and MOPAC/NMC electrodes are shown in Figures 4g,h. Both electrodes have similar curves and Ni redox couples. The oxidation peaks and reduction peaks of Ni^{2+} to $\text{Ni}^{3+}/\text{Ni}^{4+}$ appeared at 3.80 and 4.25 V, and 3.65 and

4.05 V, respectively.^[31] Since no extra peaks were observed apart from redox couples ($\text{Ni}^{2+}/\text{Ni}^{4+}$) for the MOPAC/NMC electrode, it indicates that MOPAC does not participate in electrochemical reactions. The MOPAC/NMC electrode showed a higher current for $\text{Ni}^{2+}/\text{Ni}^{4+}$ than that of the NMC electrode at higher scan rates implying a higher electrochemical activity.^[32] Electrochemical kinetics of NMC and MOPAC/NMC electrodes were analyzed by CV curves and the Randles–Sevcik equation as shown in Figure 4i. The peak current increases with increasing scan rates, and the peak current shift to high and low potentials during oxidation and reduction, respectively. This shift is due to the increased flux of ions and polarization.^[33] The Li^+ diffusion coefficient of electrodes was estimated by the Randles–Sevcik equation from CV curves at various scan rates. The peak current can be described by a function of the square root of the applied scan rate according to Equation 1.^[5c,34]

$$I_p = 2.69 \times 10^5 n^{3/2} A D_{\text{Li}}^{1/2} \nu^{1/2} C \quad (1)$$

where I_p denotes the peak current (A), n denotes the number of electrons involved in the electrochemical process, A denotes the electrode area (cm^2), D_{Li} denotes the Li diffusion coefficient ($\text{cm}^2 \text{s}^{-1}$), ν denotes the scan rate (V s^{-1}), and C denotes the concentration of Li^+ ions (mol cm^{-3}). A linear relationship between peak currents at each scan rate and the square root of applied scan rates displays Li^+ diffusion analyzed from the slope. The slopes of NMC and MOPAC/NMC electrodes obtained from the oxidation and reduction peak reveal the extraction and insertion of Li^+ for charge compensation of $\text{Ni}^{2+}/\text{Ni}^{4+}$. The MOPAC/NMC electrode shows a higher slope corresponding to high Li^+ diffusion than the NMC electrode during the redox reaction. The formation of a resistive CEI film on the NMC cathode surface exposed directly to the electrolyte slows Li^+ diffusion; this consequently increases the polarization of the electrode and reduces the peak current.^[35] Conversely, the increasing peak current and high rate of the MOPAC/NMC electrode are affected by facile interfacial Li^+ diffusion through the MOPAC film; this film simultaneously suppresses the formation of unfavorable resistive film by protecting the oxidized electrode surface from electrolyte decomposition at high charging potential.^[36]

The surface morphology of each electrode after 100 cycles was observed by SEM as shown in Figure 5a. The uneven layer on the surface of the aged NMC electrode is assumed to be the CEI layer consisting of products from electrolyte decomposition:^[37] organic species, carbonates, and transition metal fluorides (ROCO_2Li , POF^{2-} , Li_2CO_3 , LiF^{2-} , NiF_3^- , etc.). These products are deposited at the surface of the NMC, and TM dissolution is also aggravated by acidic compounds (HF).^[38] This resistive CEI film on the aged cathode impedes charge transfer at the interface at high overpotential and degrades its conductivity. Alternately, the surface morphology of the MOPAC layer remained intact on the MOPAC/NMC electrode after aging and was devoid of unwanted deposits. The homogeneous MOPAC structure constantly maintained the smooth surface layer of the electrode during the charge/discharge process by improving the interfacial stability of the electrode and preventing passivation. Thus, a stable MOPAC layer effectively suppresses the formation of a CEI layer.

The chemical composition of the outer electrode layer after 100 cycles was examined by XPS (Figure 5b). Peaks

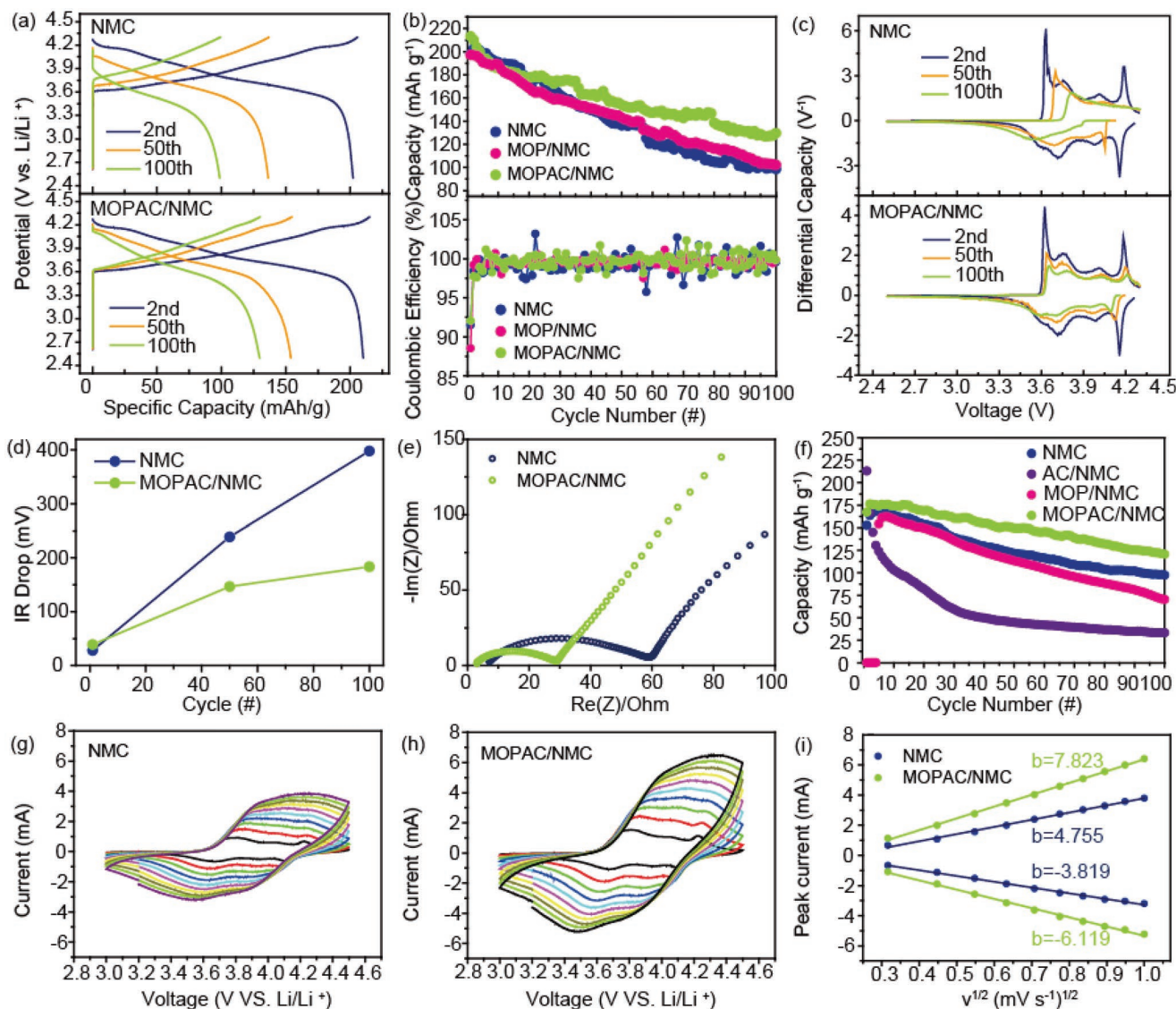


Figure 4. Electrochemical characterizations. a) Charge/discharge voltage curves of NMC and MOPAC/NMC electrodes. b) Differential capacity (dQ/dV) plots of charge/discharge curves of NMC and MOPAC/NMC electrodes. c) Cycle performances and coulombic efficiency of NMC and MOPAC/NMC cathodes at a current density of 25 mA g^{-1} . d) IR drop measurements of NMC and MOPAC/NMC cathodes after 100 cycles. e) Electrochemical impedance spectroscopy (EIS) of NMC and MOPAC/NMC cathodes after 100 cycles. f) Cycle performances of NMC, MOP/NMC, AC/NMC, and MOPAC/NMC cathodes at a current density of 250 mA g^{-1} . Cycle voltammograms of the g) NMC cathode and h) MOPAC/NMC cathode at a scan rate 0.1, 0.2, 0.3, 0.4, 0.5, 0.6, 0.7, 0.8, 0.9, and 1.0 mV s^{-1} . i) Randles–Sevcik plot of peak current versus square root of the scan rate in NMC and MOPAC/NMC cathodes.

corresponding to the binding energy of $\text{Zr}3d_{5/2}$ were observed at 184.8 and 182.2 eV for $\text{Zr}-\text{O}$ in Zr 3d spectra of MOPAC/NMC. The distinct peaks of $\text{Zr}-\text{O}$ in MOPAC indicate Zr nanoparticles that remain stable at the surface even after repeated cycles.^[39] The O 1s spectrum represents the chemical state of existing oxygen species at the electrode surface. The peak at 529 eV is attributed to the lattice oxygen of NMC, while the peak at a higher binding energy of 532.4 eV represents the active oxygen of Li_2CO_3 and LiOH . MOPAC/NMC shows a smaller intense peak for active oxygen than NMC in the O 1s region. The small peak of O^{2-} in the composite implies the reduced amount of Li_2CO_3 or LiOH at the surface after cycling.^[40]

The MOPAC film not only stabilizes the lattice oxygen of the cathode but also restrains the surface lithium residues by reducing the acid attack and electrolyte decomposition.

Ex situ XRD characterized the structural changes of NMC and MOPAC/NMC electrodes during the electrochemical process (Figure 5c). The XRD spectrum of the NMC electrode before cycling confirms a well-layered R3m structure with strong crystalline peaks representing (003) and (104) planes at 18.9° and 44.7° , respectively.^[41] The degree of cation mixing, a qualitative indication of maintenance of the layered structure, is usually determined by the ratio between integrated intensities [(003) and (104)] of peaks.^[42] The peak intensity ratio ($I_{(003)}/I_{(104)}$)

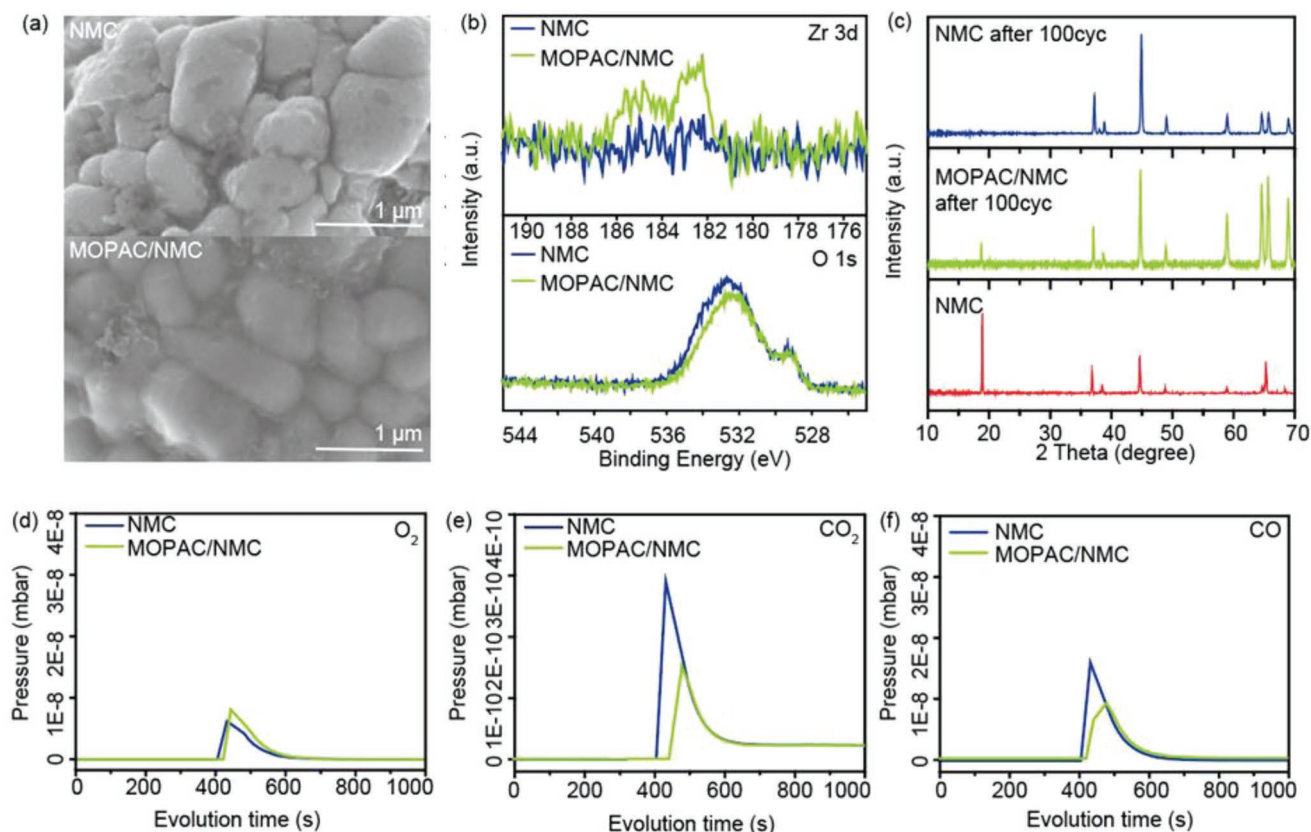


Figure 5. Ex situ measurements and DEMS analysis. a) High-resolution SEM images of NMC and MOPAC/NMC after 100 cycles. b) Ex situ XPS spectra of Zr 3d and O 1s of NMC and MOPAC/NMC after 100 cycles. c) Ex situ XRD patterns of NMC and MOPAC/NMC after 100 cycles, and the XRD patterns of NMC before cycling. Ex situ d) O₂, e) CO₂, and f) CO evolution during initial charging of NMC and MOPAC/NMC measured by DEMS.

of the NMC electrode after cycling drastically decreased from 2.19 to 0.02 as the crystallinity of the (003) plane almost disappeared. This decrease is attributed to the disruption of the R3m structure by an irreversible phase transition from H2 to H3 with active oxygen evolution generating a disordered surface area: the rock salt phase of NiO.^[43] The structural change in the MOPAC/NMC electrode was moderately aggravated since $I_{(003)}/I_{(104)}$ after cycling was 0.22. The surface protection with MOPAC restrained the Li⁺/Ni²⁺ mixing during the charge–discharge process. The MOPAC layer stabilizes the crystal structure of layered NMC and imparts superior cycling stability with rapid charge transfer and Li diffusion.

Gases produced during high voltage charging were measured for NMC and MOPAC/NMC cathodes by ex situ differential electrochemical mass spectrometry (DEMS) as shown in Figure 5d–f. The potential of NMC and MOPAC/NMC electrodes was increased up to 4.3 V after the first charging to initialize the gas evolution at the cathode by oxidation of lattice O²⁻. This produces O₂, CO₂, and CO as a result of interfacial reactions with the electrolyte (Figure S3a, Supporting Information).^[44] After initial charging, an immediate quantitative analysis of the evolved gases within the battery was conducted by integrating the pressure change of each gas. Since an equal amount of H₂ was evolved from both NMC and MOPAC/NMC electrodes, no moisture contamination was observed on the

cathode surface during the electrode fabrication (Figure S3b, Supporting Information). NMC and MOPAC/NMC electrodes showed negligible differences in the integrated areas of O₂ evolution; the MOPAC/NMC electrode exhibited a slightly higher area (Figure 5d). O₂ production at both electrodes arises from the trace concentration of saturated O₂ within the battery that remains after CO₂ and CO conversion. Hence, an almost equal amount of O₂ was detected for both samples. A noticeable difference was observed for CO₂ and CO evolution at the NMC and MOPAC/NMC electrodes as shown in Figure 5e,f. CO₂ and CO are produced at the NMC cathode by two processes: the electrolyte decomposition by releasing lattice oxygen and electrochemical oxidation of surface Li₂CO₃ at a potential above 4.25.^[16a,45] 43.7% and 16.0% less CO₂ and CO were evolved at the MOPAC/NMC cathode, respectively, than those at the NMC cathode after the initial charging. A decreased evolution of gases at the MOPAC/NMC electrode indicates that the MOPAC film successfully reduces side reactions and stabilizes the lattice oxygen by preventing the formation of lithium residues at the surface. Thus, MOPAC coating reduced major gases generated at the high voltage charging region, thus improving the lifespan of the cathode and reinforcing the safety of the battery during its operation.

The beneficial function of spray-coated MOPAC layers to improve the stability and performance of Ni-rich layered

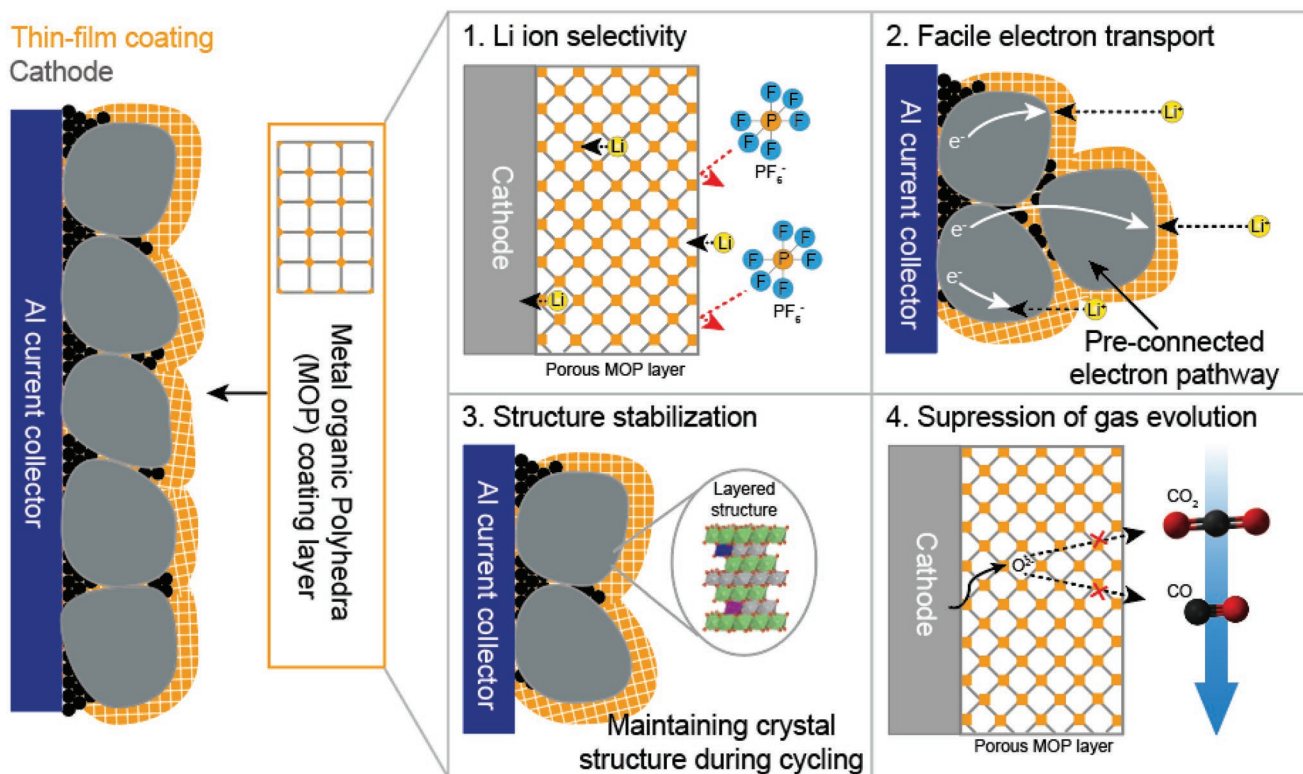


Figure 6. Schematic diagrams of functional effects of thin MOP film coated cathode achieving high performance and safety in high Ni-layered cathode.

cathodes are summarized in **Figure 6**. Uniformly and thinly deposited microporous MOPAC at the cathode surface has several advantages: i) The porous structure of MOP selectively accommodates Li^+ while preventing the absorption of unwanted electrolyte species (PF_6^-) or byproducts by the cathode surface. MOPAC pores form a selective pathway for Li^+ to diffuse toward the electrode–electrolyte interface. ii) The spray coating method enables the facile electron transport between active and conductive materials below the coating layer. The spray-coated MOPAC film creates a preconnected electron pathway, while the coating around each particle causes particle-to-particle resistance due to the thick coating layer formed along the spheres. iii) The cathode stability is achieved by the surface MOPAC film. The film blocks the degradation of the bulk cathode due to the collapsed surface structure and maintains the original structure during cycling. iv) The MOPAC layer suppresses gas evolution at the cathode during the high charging state. CO_2 and CO formation induced by O_2 evolution was significantly reduced by the MOPAC film due to the suppression of electrolyte degradation or surface lithium. Therefore, it is demonstrated that the microporous MOPAC layer is an effective coating material for the long life and safe operation of the Ni-rich layered cathode in LIBs.

3. Conclusions

In this study, dual functional coating, enabling surface stabilization and facile charge transfer on the NLC, was successfully synthesized from microporous and Li^+ selective MOPAC. The layer was added to the cathode surface by the simple spray

coating method. MOP was modified by linking acetyl chloride to form MOPAC. MOPAC was homogeneously dispersed in organic solvents and the solution was used for a thin coating of the electrode surface. The 3D porous structure was retained in the coating. The discharge capacity and cycle performance of the MOPAC-coated NLC are improved compared to those of pristine and MOP-coated cathodes as the pores of MOPAC readily accept Li ions. This aids in selective Li ion diffusion at the cathode. Simultaneously, the MOPAC film improved the structural stability of the bulk and surface of the cathode during cycling because the selective ion path in MOPAC prevents lattice degradation of the bulk structure at a high voltage. Moreover, the diffusion of the electrolyte to the cathode surface was also inhibited. The resistance and rate of the cathode were improved by the coating. The coating minimized particle-to-particle resistance and accelerated Li^+ diffusion through the tunable pores in MOPAC. The coating significantly reduced CO_2 and CO evolution when charged to a high voltage because the electrolyte decomposition and surface deterioration of cathodes were effectively suppressed. Therefore, MOPAC has several advantages as a promising cathode coating for designing safe and high-performance LIBs. We believe that the application of MOPAC coating and the spray coating method will enhance the performance of existing LIB cathodes.

4. Experimental Section

Synthesis of MOPAC: MOP crystals were prepared by Cp_2ZrCl_2 and 2-aminoterephthalic acid ($\text{H}_2\text{BDC-NH}_2$). Cp_2ZrCl_2 (17.5 mg, 0.06 mmol)

and H₂BDC-NH₂ (5.4 mg, 0.03 mmol) were dissolved in a solution of DEF (1 mL) and H₂O (150 μ L) in a 20 mL screw-capped vial. The solution was heated at 60 °C for 8 h until the formation of a yellow precipitate. The yellow precipitate was washed thrice with DEF using a centrifuge (8000 rpm for 10 min). The sample was collected by removing the solvent under vacuum and dried for 24 h at room temperature. MOP was obtained by sequentially immersing the sample in methanol for 24 h. Finally, the sample was collected by removing the solvent after 24 h using a freeze dryer.

For preparing MOPAC, MOP (10.7 mg) was dissolved in a mixture of acetonitrile (1.7 mL) and distilled water (1.7 mL) in a 20 mL vial. Triethylamine (TEA) (6.67 μ L) was added to the solution to optimize the pH of the solution until it turned pale yellow. Adipoyl chloride was added to the solution which turned transparent yellow. The mixture was heated in an oven at 120 °C for 2 days. After the completion of the reaction, a brown powdered form was obtained. The powder was washed thrice with MeOH using a centrifuge. A saturated solution of MOPAC was prepared in MeOH. This yellow transparent solution was obtained by centrifuging at 8000 rpm for 10 min.

Preparation of the MOPAC-Coated NMC: The MOPAC/NMC electrode was prepared using the spray coating method. The MOPAC solution (0.8 mg mL⁻¹) was prepared in methanol, and 2 mL of the solution was injected into a spray gun. The solution was sprayed on NMC (placed on a hotplate at 50 °C) after every 5 sec. The distance between the hotplate and spray gun was maintained at 15 cm. After coating MOPAC on NMC, the MOPAC/NMC film was obtained which was dried under vacuum for 2 h at room temperature.

Material Characterization: Powder X-ray diffraction (PXRD) patterns were obtained using a Bruker D8 Advanced (TRIO/TWIN) instrument at 1600 W (40 kV and 40 mA). X-rays were scanned at an interval of 4° per min from 5° to 20° using a silicon holder. ¹H NMR analysis of digested MOFs was detected with a Bruker Advance III HD 500 NMR spectrometer. Dried MOF powder (3 mg) was digested and dissolved in the mixture of DMSO-d₆ (700 μ L) and hydrochloric acid (200 μ L) by sonication for the sample preparation. Gas adsorption was analyzed using a BELSOPR-max (MicrotracBEL Corp.) gas adsorption analyzer. For pretreatment, samples were placed in a sample cell and dried at 120 °C for 24 h. A 77 K liquid nitrogen bath was introduced to measure N₂ sorption. Fourier transform infrared spectrophotometer (FT-IR, Nicolet IS50, Thermo Fisher Scientific) was used to investigate the structure of the synthesized MOPAC. The ATR–diamond mode was used and the IR scan range was 32 scans for 2 min. The morphology and surface of the samples were verified using a field emission scanning electron microscope (FESEM, JEM-7600F, JEOL). A focused ion beam (FIB) was performed with a Quanta3D FEG (FEI Company). Fourier Transform Raman Spectroscopy (FT–Raman, Advantec III HD500, Bruker) was used to examine the existence of MOPAC on the cathode. Measurements were obtained using a Raman module mounted in the sample compartment of the Nicolet iS50 spectrometer (Thermo Fisher Scientific Co., Waltham, MA, USA).

Electrochemical Characterization: Slurries were prepared by mixing 85 wt.% of the active material (LiNi_{0.83}Mn_{0.06}Co_{0.11}O₂, MSE Supplies LLC), 8 wt.% of the conductive material (Super-P), and 7 wt.% of a polyvinylidene fluoride (PVDF) binder in N-methylpyrrolidone (NMP) using a planetary centrifugal mixer (AR-100, MDBROS Co., Ltd.). The prepared slurries were cast on a thick doctor blade (200 mm) to achieve a nominal loading of \approx 10 mg cm⁻². The fabricated electrodes were vacuum dried at 110 °C before assembling in a cell. Coin half cells were assembled in an Ar-purged glove box (O₂ and H₂O < 0.1 ppm, MBraun, Korea) with the prepared electrodes as the working electrode (14 mm diameter), Li as the counter electrode (90 μ L of 1 M LiPF₆ in ethylene carbonate (EC)/diethyl carbonate (DEC), 1:1 by volume), 5 wt.% fluoroethylene carbonate (FEC) as the electrolyte, and Celgard 2500 sheet (diameter = 19 mm; Whatman Co., Ltd.) as the separator. Electrochemical experiments were performed at room temperature. The potentiogalvanostat (WBCS3000, WonATech, Korea) was tested for the assembled cell by applying a constant current density of 25 mA g⁻¹ in the voltage range of 2.5–4.3 V versus Li/Li⁺.

DEMS: The DEMS cell (CA-4-IWOS, Wellcos Co.) was prepared in an Ar-filled glove box. A perforated plate at the bottom of the cell and glass fiber (GF) membrane were utilized as the separator to measure the evolved gas in the coin cell system. The coin cell was sealed by a top/bottom SUS plate with a leak-free Si ring. The assembled DEMS test cell was connected to a benchtop DEMS instrument (HPR-20 R&D, HIDEN). The two Teflon tube lines of the cell were connected to the gas inlet and outlet. The outlet was connected to a mass spectrometer to monitor gas and vapor evolution. Stainless steel plates were connected to the top and bottom of the inner cell with a jig. After connecting the cells and lines, the entire line was vacuumed for 30 min to adequately remove any unnecessary components from the tube. Ar (99.999% purity), the carrier gas, with a flow of 10 cc min⁻¹ was injected into the line for 30 min to calibrate the baseline pressure by a constant gas flush. The valve was closed to collect and measure the gas that was generated from the cell. After aging, a galvanostatic charge with 25 mAh g⁻¹ was applied to the cell until its potential was 4.3 V versus Li/Li⁺. The accumulated gases in each sample during charging were detected by DEMS. The MASSoft 10 (Hiden Analytical) software was employed to acquire data and control the parameters of the mass spectrometer.

Supporting Information

Supporting Information is available from the Wiley Online Library or from the author.

Acknowledgements

Y.J.K. and S.Y.K. contributed equally to this work. This study was supported by a National Research Foundation of Korea (NRF) grant funded by the Korean government (MSIT) (Nos. 2022M3J1A1085410). This work was partly supported by the Korea Institute of Energy Technology Evaluation and Planning (KETEP) grant funded by the Korean government (MOTIE) (20221B1010003B, Integrated High-Quality Technology Development of Remanufacturing Spent Cathode for Low Carbon Resource Recirculation)

Conflict of Interest

The authors declare no conflict of interest.

Data Availability Statement

Research data are not shared.

Keywords

cathode coating, Li-ion batteries, metal–organic polyhedra, nickel-rich layered cathodes, spray coating

Received: October 24, 2022

Revised: November 5, 2022

Published online:

- [1] a) A. Manthiram, *ACS Cent. Sci.* **2017**, *3*, 1063; b) G. Zubi, R. Dufo-López, M. Carvalho, G. Pasaoglu, *Renewable Sustainable Energy Rev.* **2018**, *89*, 292; c) A. Yoshino, *Angew. Chem., Int. Ed.* **2012**, *51*, 5798; d) H.-S. Kim, B. Kim, H. Park, J. Kim, W.-H. Ryu, *Adv. Energy Mater.*

- 2022, 12, 2103527; e) H.-S. Kim, J. Lee, J. K. Yoo, W.-H. Ryu, *ACS Mater. Lett.* **2021**, 3, 815; f) Y. J. Kim, S. J. Pyo, S. Kim, W.-H. Ryu, *Carbon* **2021**, 175, 585; g) S. Kim, Y. J. Kim, W.-H. Ryu, *ACS Appl. Mater. Interfaces* **2021**, 13, 24070.
- [2] W. Li, E. M. Erickson, A. Manthiram, *Nat. Energy* **2020**, 5, 26.
- [3] a) D. S. Ko, J. H. Park, B. Y. Yu, D. Ahn, K. Kim, H. N. Han, W. S. Jeon, C. Jung, A. Manthiram, *Adv. Energy Mater.* **2020**, 10, 2001035; b) H.-H. Ryu, K.-J. Park, C. S. Yoon, Y.-K. Sun, *Chem. Mater.* **2018**, 30, 1155; c) M. Du, P. Yang, W. He, S. Bie, H. Zhao, J. Yin, Z. Zou, J. Liu, *J. Alloys Compd.* **2019**, 805, 991.
- [4] a) H. M. K. Sari, X. Li, *Adv. Energy Mater.* **2019**, 9, 1901597; b) M. Dixit, B. Markovsky, F. Schipper, D. Aurbach, D. T. Major, *J. Phys. Chem. C* **2017**, 121, 22628; c) N. W. Lee, K. R. Yoon, J. Lee, Y. Park, S. Pyo, G. Y. Kim, D. H. Ha, W.-H. Ryu, *ACS Appl. Energy Mater.* **2019**, 2, 3513.
- [5] a) J.-H. Park, K. Park, D. Han, D.-H. Yeon, H. Jung, B. Choi, S. Y. Park, S.-J. Ahn, J.-H. Park, H. N. Han, K. H. Lee, *J. Mater. Chem. A* **2019**, 7, 15190; b) S. Li, X. Fu, J. Zhou, Y. Han, P. Qi, X. Gao, X. Feng, B. Wang, *J. Mater. Chem. A* **2016**, 4, 5823; c) L. Yao, F. Liang, J. Jin, B. V. R. Chowdari, J. Yang, Z. Wen, *Chem. Eng. J.* **2020**, 389, 124403; d) X. Zhang, A. Chen, M. Zhong, Z. Zhang, X. Zhang, Z. Zhou, X.-H. Bu, *Electrochem. Energy Rev.* **2018**, 2, 29; e) H. Furukawa, K. E. Cordova, M. O'Keeffe, O. M. Yaghi, *Science* **2013**, 341; f) A. E. Baumann, D. A. Burns, B. Liu, V. S. Thoi, *Communications Chemistry* **2019**, 2, 86; g) G. Huang, D. M. Yin, L. M. Wang, *J. Mater. Chem. A* **2016**, 4, 15106; h) H.-C. Zhou, J. R. Long, O. M. Yaghi, *Chem. Rev.* **2012**, 112, 673; i) P. Deria, J. E. Mondloch, O. Karagiari, W. Bury, J. T. Hupp, O. K. Farha, *Chem. Soc. Rev.* **2014**, 43, 5896.
- [6] a) Y. Kim, T. Yang, G. Yun, M. B. Ghasemian, J. Koo, E. Lee, S. J. Cho, K. Kim, *Angew. Chem.* **2015**, 127, 13471; b) Y. Furukawa, T. Ishiwata, K. Sugikawa, K. Kokado, K. Sada, *Angew. Chem., Int. Ed.* **2012**, 51, 10566; c) Z. Li, X. Ge, C. Li, S. Dong, R. Tang, C. Wang, Z. Zhang, L. Yin, *Small Methods* **2020**, 4, 1900756; d) D. R. Du Bois, A. J. Matzger, *J Am Chem Soc* **2020**, 143, 671.
- [7] a) M. Kalaj, K. C. Bantz, S. Ayala, J. M. Palomba, K. S. Barcus, Y. Katayama, S. M. Cohen, *Chem. Rev.* **2020**, 120, 8267; b) L. Chen, Q. Xu, *Matter* **2019**, 1, 57; c) G. Cai, P. Yan, L. Zhang, H.-C. Zhou, H.-L. Jiang, *Chem. Rev.* **2021**, 121, 12278.
- [8] a) H. S. Lee, S. Jee, R. Kim, H.-T. Bui, B. Kim, J.-K. Kim, K. S. Park, W. Choi, W. Kim, K. M. Choi, *Energy Environ. Sci.* **2020**, 13, 519; b) D. Nam, J. Huh, J. Lee, J. H. Kwak, H. Y. Jeong, K. Choi, W. Choe, *Chem. Sci.* **2017**, 8, 7765; c) S. Kim, S. Jee, K. M. Choi, D.-S. Shin, *Nano Res.* **2020**, 14, 486; d) X. Guo, S. Xu, Y. Sun, Z. Qiao, H. Huang, C. Zhong, *J. Membr. Sci.* **2021**, 632, 119354; e) S. Mollick, S. Fajal, S. Mukherjee, S. K. Ghosh, *Chem Asian J* **2019**, 14, 3096; f) X. Liu, X. Wang, A. V. Bavykina, L. Chu, M. Shan, A. Sabetghadam, H. Miro, F. Kapteijn, J. Gascon, *ACS Appl. Mater. Interfaces* **2018**, 10, 21381.
- [9] W. Zhu, A. Li, Z. Wang, J. Yang, Y. Xu, *Small* **2021**, 17, 2006424.
- [10] M. A. Andrés, A. Carné-Sánchez, J. Sánchez-Lainez, O. Roubeau, J. Coronas, D. MasPOCH, I. Gascón, *Chemistry* **2019**, 26, 143.
- [11] a) G. Liu, X. Zhang, Y. Di Yuan, H. Yuan, N. Li, Y. Ying, S. B. Peh, Y. Wang, Y. Cheng, Y. Cai, Z. Gu, H. Cai, D. Zhao, *ACS Mater. Lett.* **2021**, 3, 268; b) M. Zhang, Y. Lai, M. Li, T. Hong, W. Wang, H. Yu, L. Li, Q. Zhou, Y. Ke, X. Zhan, T. Zhu, C. Huang, P. Yin, *Angew. Chem.* **2019**, 131, 17573; c) M. Li, M. Zhang, Y. Lai, Y. Liu, C. Halbert, J. F. Browning, D. Liu, P. Yin, *J. Phys. Chem. C* **2020**, 124, 15656.
- [12] a) L. Liang, Q. Zhu, L. Shi, F. Wang, J. Ma, J. Sun, *J. Porous Mater.* **2014**, 21, 985; b) N. Delaporte, A. Darwiche, M. Léonard, G. Lajoie, H. Demers, D. Clément, R. Veillette, L. Rodrigue, M. L. Trudeau, C. Kim, K. Zaghib, *Sci. Rep.* **2020**, 10, 11813; c) M. Serwar, U. A. Rana, H. M. Siddiqi, S. Ud-Din Khan, F. A. Ahmed Ali, A. Al-Fatesh, A. Adomkevicius, J. A. Coca-Clemente, L. Cabo-Fernandez, F. Braga, L. J. Hardwick, *RSC Adv.* **2017**, 7, 54626; d) T.-H. Chen, L. Wang, J. V. Trueblood, V. H. Grassian, S. M. Cohen, *J. Am. Chem. Soc.* **2016**, 138, 9646.
- [13] a) R. R. N. D. Bosubabu, K. B. M. G. K. Ramesha, *ACS Appl. Energy Mater.* **2020**, 3, 10872; b) Y. Chen, W. Zhao, Q. Zhang, G. Yang, J. Zheng, W. Tang, Q. Xu, C. Lai, J. Yang, C. Peng, *Adv. Funct. Mater.* **2020**, 30, 2000396; c) H. Wang, X. Li, F. Li, X. Liu, S. Yang, J. Ma, *Electrochem. Commun.* **2021**, 122, 106870.
- [14] a) R. Jung, R. Morasch, P. Karayaylali, K. Phillips, F. Maglia, C. Stinner, Y. Shao-Horn, H. A. Gasteiger, *J. Electrochem. Soc.* **2018**, 165, A132; b) R. Jung, F. Linsenmann, R. Thomas, J. Wandt, S. Solchenbach, F. Maglia, C. Stinner, M. Tromp, H. A. Gasteiger, *J. Electrochem. Soc.* **2019**, 166, A378; c) W. Zhao, J. Zheng, L. Zou, H. Jia, B. Liu, H. Wang, M. H. Engelhard, C. Wang, W. Xu, Y. Yang, J. G. Zhang, *Adv. Energy Mater.* **2018**, 8, 1800297.
- [15] a) L. de Biasi, B. Schwarz, T. Brezesinski, P. Hartmann, J. Janek, H. Ehrenberg, *Adv. Mater.* **2019**, 31, 1900985; b) C. Wang, L. Xing, J. Vatamanu, Z. Chen, G. Lan, W. Li, K. Xu, *Nat. Commun.* **2019**, 10, 3423.
- [16] a) S. S. Zhang, *Energy Storage Mater.* **2020**, 24, 247; b) Q. Li, Z. Li, S. Wu, Z. Wang, X. Liu, W. Li, N. Li, J. Wang, W. Zhuang, *ACS Appl. Energy Mater.* **2020**, 3, 11741; c) Y. J. Kim, G.-Y. Kim, H.-S. Kim, S. Kim, B. Kim, Y. J. Choi, J. Kim, J. Kim, W.-H. Ryu, *Composites, Part B* **2022**, 238, 109911.
- [17] H. Kim, M. G. Kim, H. Y. Jeong, H. Nam, J. Cho, *Nano Lett.* **2015**, 15, 2111.
- [18] a) R. Jung, M. Metzger, F. Maglia, C. Stinner, H. A. Gasteiger, *J. Electrochem. Soc.* **2017**, 164, A1361; b) W. Li, S. Lee, A. Manthiram, *Adv. Mater.* **2020**, 32, 2002718; c) C. Xu, P. J. Reeves, Q. Jacquet, C. P. Grey, *Adv. Energy Mater.* **2021**, 11, 2003404.
- [19] T. Liu, L. Yu, J. Lu, T. Zhou, X. Huang, Z. Cai, A. Dai, J. Gim, Y. Ren, X. Xiao, M. V. Holt, Y. S. Chu, I. Arslan, J. Wen, K. Amine, *Nat. Commun.* **2021**, 12, 6024.
- [20] a) H. Li, A. Liu, N. Zhang, Y. Wang, S. Yin, H. Wu, J. R. Dahn, *Chem. Mater.* **2019**, 31, 7574; b) J.-H. Kim, H.-H. Ryu, S. J. Kim, C. S. Yoon, Y.-K. Sun, *ACS Appl. Mater. Interfaces* **2019**, 11, 30936.
- [21] a) F. Wu, N. Liu, L. Chen, Y. Su, G. Tan, L. Bao, Q. Zhang, Y. Lu, J. Wang, S. Chen, J. Tan, *Nano Energy* **2019**, 59, 50; b) L. Li, J. Chen, H. Huang, L. Tan, L. Song, H.-H. Wu, C. Wang, Z. Zhao, H. Yi, J. Duan, T. Dong, *ACS Appl. Mater. Interfaces* **2021**, 13, 42554.
- [22] J. Song, S. Oh, S. Lee, J.-J. Woo, S. Choi, I.-C. Jang, *J. Electrochem. Soc.* **2021**, 168, 090542.
- [23] J. Hu, B. Wu, X. Cao, Y. Bi, S. Chae, C. Niu, B. Xiao, J. Tao, J. Zhang, J. Xiao, *J. Power Sources* **2020**, 454, 227966.
- [24] a) X. Li, J. Liu, M. N. Bani, A. Lushington, R. Li, M. Cai, X. Sun, *Energy Environ. Sci.* **2014**, 7, 768; b) U. Nisar, R. Petla, S. A. Jassim Al-Hail, A. A. Quddus, H. Monawwar, A. Shakoore, R. Essehli, R. Amin, *RSC Adv.* **2020**, 10, 15274.
- [25] a) Y. Su, S. Cui, Z. Zhuo, W. Yang, X. Wang, F. Pan, *ACS Appl. Mater. Interfaces* **2015**, 7, 25105; b) P.-C. Tsai, B. Wen, M. Wolfman, M.-J. Choe, M. S. Pan, L. Su, K. Thornton, J. Cabana, Y.-M. Chiang, *Energy Environ. Sci.* **2018**, 11, 860.
- [26] a) A. M. Wise, C. Ban, J. N. Weker, S. Misra, A. S. Cavanagh, Z. Wu, Z. Li, M. S. Whittingham, K. Xu, S. M. George, M. F. Toney, *Chem. Mater.* **2015**, 27, 6146; b) H. Nara, K. Morita, D. Mukoyama, T. Yokoshima, T. Momma, T. Osaka, *Electrochim. Acta* **2017**, 241, 323.
- [27] a) Z. Chen, Y. Qin, K. Amine, Y. K. Sun, *J. Mater. Chem.* **2010**, 20, 7606; b) H. Hemmelmann, J. K. Dinter, M. T. Elm, *Adv. Mater. Interfaces* **2021**, 8, 2170047.
- [28] E. Billy, M. Joulié, R. Laucournet, A. Boulineau, E. De Vito, D. Meyer, *ACS Appl. Mater. Interfaces* **2018**, 10, 16424.
- [29] L. Liu, Q. Wan, C. Gui, P. He, Z. Zhao, Z. Wang, B.-Z. Tang, *Chem. Commun.* **2022**, 58, 5769.

- [30] a) M. A. H. Shuva, A. S. W. Kurny, *Journal of The Institution of Engineers (India): Series D* **2013**, *94*, 13; b) W. Xuan, A. Otsuki, A. Chagnes, *RSC Adv.* **2019**, *9*, 38612.
- [31] a) Q. Guo, J. Huang, Z. Liang, H. Potapenko, M. Zhou, X. Tang, S. Zhong, *New J. Chem.* **2021**, *45*, 3652; b) M. Zhang, H. Zhao, M. Tan, J. Liu, Y. Hu, S. Liu, X. Shu, H. Li, Q. Ran, J. Cai, X. Liu, *J. Alloys Compd.* **2019**, *774*, 82.
- [32] M. R. Laskar, D. H. K. Jackson, S. Xu, R. J. Hamers, D. Morgan, T. F. Kuech, *ACS Appl. Mater. Interfaces* **2017**, *9*, 11231.
- [33] F. Wu, J. Dong, L. Chen, L. Bao, N. Li, D. Cao, Y. Lu, R. Xue, N. Liu, L. Wei, Z. Wang, S. Chen, Y. Su, *Energy Storage Mater.* **2021**, *41*, 495.
- [34] H. Sun, Z. Cao, T. Wang, R. Lin, Y. Li, X. Liu, L. Zhang, F. Lin, Y. Huang, W. Luo, *Mater. Today Energy* **2019**, *13*, 145.
- [35] a) S. Deng, X. Li, Z. Ren, W. Li, J. Luo, J. Liang, J. Liang, M. N. Bani, M. Li, Y. Zhao, X. Li, C. Wang, Y. Sun, Q. Sun, R. Li, Y. Hu, H. Huang, L. Zhang, S. Lu, J. Luo, X. Sun, *Energy Storage Mater.* **2020**, *27*, 117; b) L. Li, D. Wang, G. Xu, Q. Zhou, J. Ma, J. Zhang, A. Du, Z. Cui, X. Zhou, G. Cui, *J Energy Chem* **2022**, *65*, 280.
- [36] Q. Li, Y. Wang, X. Wang, X. Sun, J.-N. Zhang, X. Yu, H. Li, *ACS Appl. Mater. Interfaces* **2019**, *12*, 2319.
- [37] R. S. Negi, S. P. Culver, M. Wiche, S. Ahmed, K. Volz, M. T. Elm, *Phys. Chem. Chem. Phys.* **2021**, *23*, 6725.
- [38] a) Q. Wu, S. Mao, Z. Wang, Y. Tong, Y. Lu, *Nano Select* **2020**, *1*, 111; b) X. Fan, G. Hu, B. Zhang, X. Ou, J. Zhang, W. Zhao, H. Jia, L. Zou, P. Li, Y. Yang, *Nano Energy* **2020**, *70*, 104450.
- [39] J.-Z. Kong, S.-S. Wang, G.-A. Tai, L. Zhu, L.-G. Wang, H.-F. Zhai, D. Wu, A.-D. Li, H. Li, *J. Alloys Compd.* **2016**, *657*, 593.
- [40] Y. Su, L. Li, G. Chen, L. Chen, N. Li, Y. Lu, L. Bao, S. Chen, F. Wu, *Chin. J. Chem.* **2020**, *39*, 189.
- [41] J. Yang, Y. Xia, *ACS Appl. Mater. Interfaces* **2016**, *8*, 1297.
- [42] Z. Tang, J. Bao, Q. Du, Y. Shao, M. Gao, B. Zou, C. Chen, *ACS Appl. Mater. Interfaces* **2016**, *8*, 34879.
- [43] J. Shu, R. Ma, L. Shao, M. Shui, K. Wu, M. Lao, D. Wang, N. Long, Y. Ren, *J. Power Sources* **2014**, *245*, 7.
- [44] H. Wang, E. Rus, T. Sakuraba, J. Kikuchi, Y. Kiya, H. D. Abruña, *Anal. Chem.* **2014**, *86*, 6197.
- [45] T. Hatsukade, A. Schiele, P. Hartmann, T. Brezesinski, J. Janek, *ACS Appl. Mater. Interfaces* **2018**, *10*, 38892.